

# Quantum Resources Required for Binding Affinity Calculations of Amyloid beta

Matthew Otten,<sup>1,2</sup> Thomas W. Watts,<sup>3</sup> Samuel D. Johnson,<sup>3</sup> Rashmi Sundareswara,<sup>3</sup> Zhihui Wang,<sup>4,5</sup> Tarini S. Hardikar,<sup>6</sup> Kenneth Heitritter,<sup>6</sup> James Brown,<sup>6</sup> Kanav Setia,<sup>6</sup> and Adam Holmes<sup>3,7</sup>

<sup>1</sup>*Department of Physics, University of Wisconsin – Madison, Madison, WI, USA*

<sup>2</sup>*Corresponding author: mjotten@wisc.edu*

<sup>3</sup>*HRL Laboratories, LLC, Malibu, CA, USA*

<sup>4</sup>*Quantum Artificial Intelligence Laboratory (QuAIL),*

*NASA Ames Research Center, Moffett Field, CA*

<sup>5</sup>*Research Institute for Advanced Computer Science (RIACS), USRA, Moffett Field, CA*

<sup>6</sup>*qBraid Co., 111 S Wacker Dr., Chicago, IL 60606, USA*

<sup>7</sup>*Corresponding author: aholmes@hrl.com*

Amyloid beta, an intrinsically disordered protein, plays a seemingly important but not well-understood role in neurodegenerative diseases like Alzheimer’s disease. A key feature of amyloid beta, which could lead to potential therapeutic intervention pathways, is its binding affinity to certain metal centers, like iron and copper. Numerically calculating such binding affinities is a computationally challenging task, involving strongly correlated metal centers. A key bottleneck in understanding the binding affinity is obtaining estimates of the ground state energy. Quantum computers have the potential to accelerate such calculations but it is important to understand the quantum resources required. In this work, we detail a computational workflow for binding affinity calculations for amyloid beta utilizing quantum algorithms, providing estimated quantum resources required, at both the logical and hardware level.

## I. INTRODUCTION

Proteins which contain a metal ion cofactor, known as metalloproteins, account for nearly half of all proteins in nature, with functions ranging from photosynthesis to nitrogen fixation to important biological functions [1]. Metal protein interactions represent a strongly correlated system, where standard classical electronic structure techniques fail to accurately predict features such as coordination and dynamics [2]. Quantum computers have long been predicted to be able to solve such strongly correlated problems exponentially faster than classical computers [3]. In fact, nitrogenase, which serves as an important protein in natural nitrogen fixation, through its primary cofactor, iron molybdenum cofactor (FeMo-co), has long served as an example of a problem that future, fault-tolerant quantum computers may be able to solve and is often used as a basis for quantum resource estimation [4–6].

In their biological function, certain metalloproteins, specifically the protein amyloid beta ( $A\beta$ ) interacting with metal ions such as copper, iron, and zinc, have been linked to neurodegenerative diseases such as Alzheimer’s disease [7]. These interactions have been studied via many classical techniques, including molecular dynamics (MD), quantum mechanics / molecular mechanics (QM/MM), and density functional theory (DFT) [8], but a lack of accuracy has resulted in conflicting predictions for coordination schemes and other chemical quantities. Higher accuracy

calculations are therefore necessary to fully understand  $A\beta$ ’s role in the onset of neurodegenerative diseases. In this paper, we provide specific instances of  $A\beta$ -metal ion systems and further provide estimates of the required quantum resources to perform accurate calculations on such systems.

## II. PROBLEM STATEMENT AND UTILITY

Amyloid-beta is a protein that is critical to understanding the pathogenesis of Alzheimer’s Disease (AD). Created by proteases breaking down Amyloid Precursor Protein (APP), Amyloid-Beta ( $A\beta$ ) is a disordered protein and the subject of many leading AD hypotheses. Chief among these hypotheses is the amyloid cascade hypothesis and the oligomer cascade hypothesis (are soluble low molecular weight oligomers causing toxicity or is it the abnormal accumulation of plaques in the brain? [9]). To understand this aggregation and to design targeted drugs, a key challenge is understanding how  $A\beta$  interacts with metal ions such as zinc, copper, iron, and platinum [10, 11].

Therefore, it is important to correctly model these metalloproteins and calculate their metal binding affinities. There are many possible metal-binding domains that could be studied; AB16 (shown in Fig. 1) is considered the minimal metal-binding domain for the larger  $A\beta$  protein (Protein Databank (PDB) ID: 1ZE9) [12]. At physiologically relevant conditions (pH 6.5), many possible

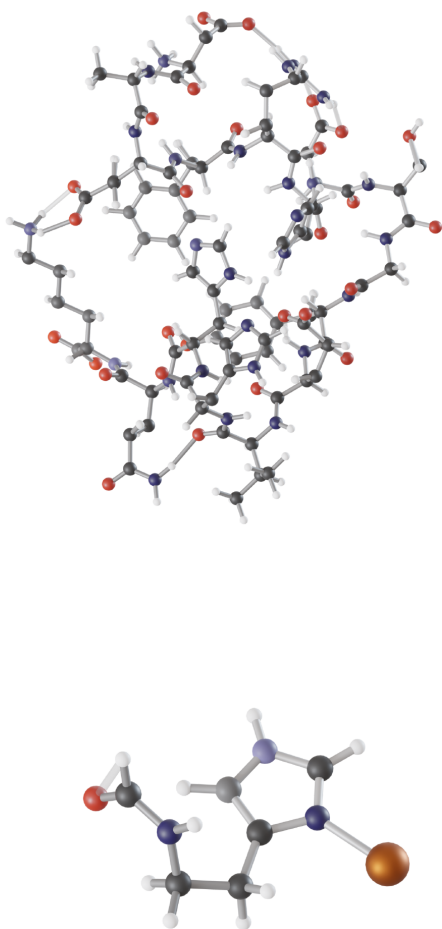


FIG. 1. Top: The full structure of the AB16 protein. Bottom: A possible binding site (His6) with a Cu metal ion.

different binding sites are found for AB16. Nuclear magnetic resonance (NMR) studies support His6, His13, His14, and Glu11 as the binding sites [12]; one such region, His6, is shown interacting with a copper ion in Fig. 1. Experimental studies are faced with the challenges of highly disordered structure, the rapid kinetics of aggregation, and solvent effects when identifying coordination schemes, demonstrating the need for computational tools. Computational studies have been performed on AB16, with a variety of techniques used, such as QM/MM, classical MD, and DFT. Each approach has its own shortcomings, and often suggests alternative coordination schemes such as with oxygen, COAla2, Tyr10, Asp1, N-terminal nitrogen, or even water as the fourth coordination site [8]. The specific computational

task is to calculate the metal binding affinity of the AB16 protein. The specific process for calculating this is detailed in the workflow below. Knowing the metal binding affinity provides insight into how AB16 interacts with metal ions and can be used to inform a broader theory to understand its role in plaque aggregation and to potentially design targeted drugs. For instance, a correct understanding of metal-protein coordination sites can allow us to understand the mechanism and kinetics of protein oligomerization and aggregation, show what ions contribute to this effect, and what physiological factors are necessary for this process to occur. A binding energy based mechanistic understanding can be the key to studying one of the earliest points of AD diagnosis. This, in turn, can be useful in future drug discovery and design pipelines, which could help alleviate the burden of AD. The specific problem we study, that of the AB16 protein, is only one in a family of possible  $A\beta$  metalloproteins. Larger proteins (such as AB40 or AB42) could also be potential computational targets. The larger set of metalloproteins also include systems important for photosynthesis, nitrogen fixation, and water oxidation [1]. The techniques described here for AB16 could be applied to the wider family of metalloproteins.

Alzheimer’s disease has a large economic impact; the Alzheimer’s Association reported that in 2024 the total payments for health care, long-term care and hospice services for people age 65 and older with dementia was estimated to be \$360 billion [13]. It is certainly not expected that calculations of the metal-binding affinity of AB16 will directly lead to a therapeutic for AD. To attempt to quantify the potential utility of a successful computational solution for the metal-binding affinity in  $A\beta$ , we instead look at the National Institutes of Health (NIH) RePORTER tool, which reports, among other things, the research expenditures of the NIH in an open, searchable manner [14]. Since 2005, the NIH has spent around \$8.9 billion on awards for projects mentioning ‘amyloid beta’ (and other variants, such as ‘beta amyloid’). From that set of awards, a total of around \$280 million mention the word ‘computational’ in the abstract. Therefore, we estimate that a technique or device which could solve the computational problems detailed in this paper would have a utility of at least \$280 million.

### III. WORKFLOW

For this application, the goal is to understand how  $A\beta$  interacts with various metal ions. While there are many ways to attack this problem, one workflow, following the quantum mechani-

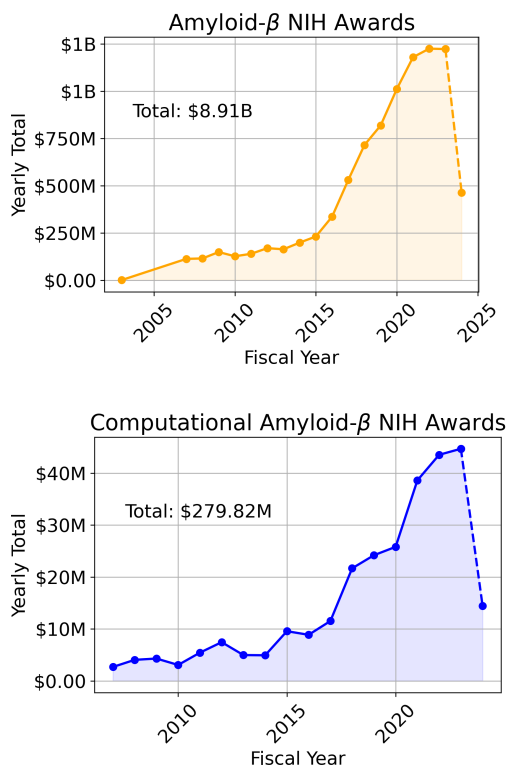


FIG. 2. Funded NIH awards per fiscal year. Top: All awards mentioning amyloid- $\beta$  and variants ( $\beta$ -amyloid, ect). Bottom: Amyloid- $\beta$  awards with “computational” in the abstract.

cal/molecular mechanics (QM/MM) approach is as follows [15]. First, an experimental or previously studied geometry is taken from a database, such as the protein database. Specific choices for this geometry (such as the AB16 protein) are discussed elsewhere. This structure is then reoptimized at a coarse level (that of, say, classical force fields) using geometry optimization techniques. This level of optimization results in several local minima of similar quality, which are then chosen to be analyzed at more detailed level of theory, here using a QM/MM approach. The QM/MM performs additional optimization, where a small region is treated fully quantum mechanically (at, say, a hybrid functional DFT level), and the rest of the protein is treated via molecular mechanics. The various geometries found from this additional optimization are then analyzed at an even more accurate level of theory. Here, we use the fragment molecular orbital (FMO) [16] method to divide the AB16 protein into multiple smaller fragments. The ground state energy of these fragments is then found directly using the most accurate level of theory (either a full configuration interaction (FCI)-like algorithm on classical computers or a quantum phase estimation (QPE) al-

gorithm on quantum computers). The energies of each fragment are combined via the FMO algorithm to get the overall energy for the various conformations (geometries). These energies are compared to determine which conformations are most energetically favorable. The metal binding affinity can then be calculated by comparing the energy of the protein (which would be calculated via a similar QM/MM technique) with and without the additional metal ions. Several corrections to the energy, such as dispersion and solvation, may be applied. This workflow is show diagrammatically in Fig. 3.

The accuracy afforded at the lowest level of the calculation, at the individual fragment level, is necessary to distinguish between multiple possible structures. QM/MM techniques have been applied to the A $\beta$  system before, using much less accurate techniques compared with the proposed FMO + FCI or QPE method. One study, using such less-accurate techniques, found 8 structures, all lying within about 40 kJ/mol of each other, which, due to an expected accuracy of only  $\sim$ 20 kJ/mol, had to all be considered equally probable [15]. Overall, the energy of dozens of geometries, both with and without an additional metal ion, need to be calculated in an optimization / dynamical loop, resulting in hundreds of energy evaluations each.

### A. Specific Hamiltonian

We use the AB16 protein (PDB ID:1ZE9) [12] as our protein of interest. The choice for the specific protein structure is motivated by the fact that it is the minimal metal coordination domain within the larger AB42 structure. With a structure identified at physiologically relevant pH by solution NMR, AB16 is realistic and biologically relevant starting point. Furthermore, this structure has been previously studied using classical techniques, showcasing interest from the community as well as previous results to benchmark against. The atomic structure of AB16 is shown in Fig. 1. As part of our workflow, we divide the protein into individual fragments which are solved separately and whose solutions are combined classically. The most interesting, and likely most difficult, fragments to solve are the ones which involve the metal ion. One such potential binding site, His6, with a copper ion, is shown in Fig. 1. Our fragmentation scheme results in 15 fragments.

Given the positions of the atoms, we represent our Hamiltonian using Gaussian type orbitals (GTO). To provide a wide range of resource estimates, we use several basis sets, including, in order of increasing numbers of basis functions,

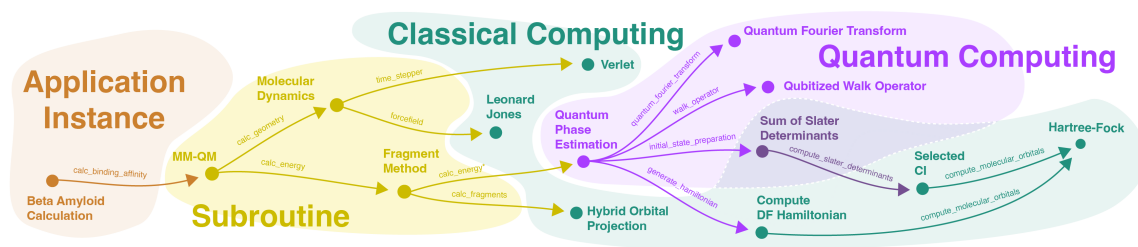


FIG. 3. Quantum benchmarking graph (QBG) of the proposed computational workflow.

STO-3G, 6-31g\* and cc-pvdz. The largest basis sets (Dunning’s correlation consistent basis sets [17]) studied here are consistent with those that are used for highly-accurate quantum chemistry studies. No active space is used; we directly correlate all electrons.

## B. Specific Algorithm Descriptions

### 1. Fragment Molecular Orbital

The first step in the pipeline is generating fragments from the larger protein sequence. This is done using Fragment Molecular Orbital (FMO) method [18]. This method preserves chemical information by breaking bonds heterolytically and moving a bond with a proton. The method follows an energy decomposition approach, where the energy of the entire molecule is constructed by summing over monomer fragment energies, dimer fragment energies, and so on. Overlapping fragment energies are then subtracted. At the monomer step, each monomer’s electronic density relaxes with respect to the electric field of all other monomers, and are recalculated until a self consistent cycle converges. At the dimer step, dimer energies are calculated in the field of the monomer densities (which are not recalculated) [19].

### 2. Quantum Phase Estimation with Double-Factorized Qubitization

Quantum phase estimation (QPE) is one of the core algorithms for solving quantum chemistry problems on quantum computers [20]. The QPE algorithm to estimate the eigenvalue for a unitary  $U$  can be characterized by the following key steps:

- **Initialization.** The algorithm starts with two registers. The ancilla register is initialized to  $\otimes |+\rangle$  state. The data register is prepared in a state that has suitable over-

lap with the desired eigenstate of the unitary operator  $U$ .

- **Controlled Unitary Operations.** A series of controlled unitary operations  $U^{2^k}$  with integer  $k$  are applied to the data register, conditioned on the state of the ancilla qubits. By varying  $k$  for each operation, different powers of the phase are encoded (phase kick-back) into the ancilla qubits. Implementation of controlled unitaries in this step constitutes the major contribution to resource estimation.
- **Inverse Quantum Fourier Transform (QFT).** The ancilla register now is in a superposition state encoding the eigenvalue of  $U$ . The inverse Quantum Fourier Transform is then applied to this register and upon measuring the ancilla register, one get a bit string that is an estimate of the phase of the eigenvalue of  $U$ . The desired accuracy of the phase estimate determines the number of ancilla qubits needed and hence is a key factor for resource estimation.

For QPE to be applied for ground state energy estimation, an initial state with suitable overlap with the ground state is prepared and evolved in time under the action of the Hamiltonian,  $H$ . Various methods of time-evolution can be used, including Trotterization [21, 22] and qubitization [23]. We use the double-factorized qubitization algorithm of Ref. [24]. In qubitization, the time evolution is performed not through the direct Hamiltonian,  $H$ , but instead through a walk operator,  $W = e^{i \sin^{-1}(H)}$  [23]. Compared with the Trotterization of the time-evolution unitary  $\exp[-itH]$ , qubitization provides a considerable reduction in gate depth at the cost of additional logical qubits. The technique of qubitization holds great promises for molecular systems in terms of the T-gate complexity.[25, 26] For our specific amyloid- $\beta$  application, we use the stan-

standard quantum chemistry electronic Hamiltonian,

$$H = \sum_{ij,\sigma} h_{ij} a_{(i,\sigma)}^\dagger a_{(i,\sigma)} + \frac{1}{2} \sum_{ijkl,\sigma\rho} h_{ijkl} a_{(i,\sigma)}^\dagger a_{(k,\rho)}^\dagger a_{(l,\rho)} a_{(j,\sigma)}, \quad (1)$$

where  $h_{ij}$  and  $h_{ijkl}$  are the one- and two-electron integrals (computed via a standard quantum chemistry package, e.g., pyscf [27]);  $\sigma$  and  $\rho$  index spin; and  $a_p$  are Fermion raising and lowering operators. The Hamiltonian, eq. (1), is decomposed through the so-called double-factorization procedure,

$$H_{DF} = \sum_{ij,\sigma} \bar{h}_{ij} a_{i,\sigma}^\dagger a_{j,\sigma} + \frac{1}{2} \sum_{r \in [R]} \left( \sum_{ij,\sigma} \sum_{m \in [M^{(r)}]} \lambda_m^{(r)} \bar{R}_{m,i}^{(r)} \bar{R}_{m,j}^{(r)} a_{i,\sigma}^\dagger a_{j,\sigma} \right)^2. \quad (2)$$

This expression is derived from Eq. 1 through a two-step factorization of the two-electron tensor terms. We refer the readers to Ref. [24] for the derivation and more details.

Using Majorana representation of fermion operators, the double-factored Hamiltonian  $H_{DF}$  is mapped into a sum of squares of one-body Hamiltonians, and the walk operator can then be synthesized.

#### IV. RESOURCE ESTIMATES

We estimate the quantum resources required to solve for the ground state energy of each fragment using the Azure Quantum Resource Estimator [28, 29] implemented in the Azure Quantum Development Kit [30]. For logical resource estimates, we use an accuracy cutoff of 1mHa, slightly below chemical accuracy for the double-factorized qubitization algorithm. For physical resource estimates, we use a model consistent with error rates and gate times for optimistic superconducting qubits implementing a surface code with a total error budget of 1%.

##### 1. Resource Estimation Details

We use the Azure Quantum Resource Estimator (AzureQRE) [29] to provide both the logical and physical resource estimates. We briefly describe several important features of the Azure QRE here; more details can be found in Ref. [28]. The AzureQRE takes the definition of a logical circuit and compiles it into a Quantum Intermediate Representation. At the physical level, it assumes a 2D nearest-neighbor layout that has the

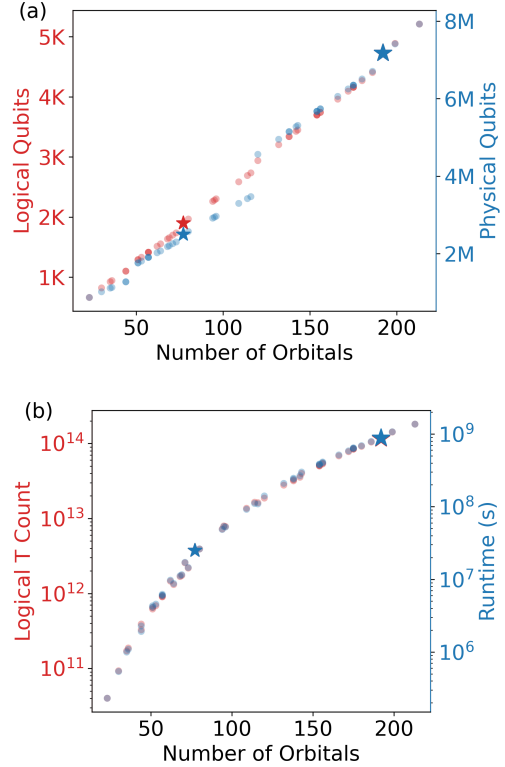


FIG. 4. Resource estimates for all fragments of AB16 using various basis sets. Stars represent resource estimates that include a metal center, where we expect we need the accuracy provided by a quantum computer. (a) Number of physical and logical qubits. The step in the number of physical qubits is due to an increase in the surface code distance,  $d$ . (b) Logical T count and total runtime. A table of all estimates, including other information like surface code distance, number of T factories, etc, can be found in the appendix.

ability to perform parallel operations. Because the qubits are inherently noisy, we must estimate the overhead of quantum error correction; specifically, we estimate the overhead using the surface code [31]. The distance,  $d$ , of the surface code parameterizes the level of error suppression and is adjusted based on the logical depth and physical qubit parameters. Logical qubit movement and multi-qubit measurements are assumed to be performed via lattice surgery operations. The cost to implement T gates is estimated via the use of T state distillation factories [32]. We use physical qubit parameters consistent with an optimistic superconducting qubit device, with 50 ns gate times, 100 ns measurement times, and  $10^{-4}$  Clifford and non-Clifford error rates. Within the AzureQRE, this has the name `qubit_gate_ns_e4`.



## 2. Resource Estimation Results

Logical resource estimates are shown in Fig. 4 for all 15 fragments over the various basis sets. The specific estimates for the fragments containing metal ions are shown with stars; these fragments are the ones expected to have the strongest correlation, necessitating the accuracy provided by quantum computers. The number of logical qubits necessary grows linearly with the number of orbitals; the total number of qubits needed is about an order of magnitude larger than the number of orbitals used to represent the problem due to the additional ancilla qubits needed to perform the double-factorized qubitization algorithm. The number of logical T gates grows clearly as  $O(n^5)$ , with no clear difference between the fragments with and without the metal ion. To calculate the His6 binding site with a copper ion in the 6-31g\* basis set, we estimate that 4728 logical qubits implementing  $1.17e14$  T gates would be required to perform the double-factorized qubitization algorithm. This system is potentially the smallest system of practical interest, with 192 orbitals. The 6-31g\* basis set is the smallest basis set that has the potential to provide somewhat accurate results, though larger basis sets are likely needed to lower the basis set error.

To perform such a deep circuit, quantum error correction will be necessary. Physical resource estimates, utilizing quantum error correction, are shown in Fig. 4. The total number of physical qubits is now in the millions. For the His6 binding site with a copper ion in the 6-31g\* basis set, 7 million physical qubits would be required, with an estimated runtime of 8.8e8s, a little over 28 years.

## V. CONCLUSION

In this paper, we provide a specific example of a biologically-relevant, computational metal-organic problem: calculating the metal-binding

affinity of the AB16 protein, which is relevant for the study of A $\beta$ 's role in neurodegenerative diseases, such as Alzheimer's disease. Through a specific computational workflow, involving QM/MM, FMO, and QPE, we provide detailed quantum resource estimates for solving this problem. The utility of solving this computational problem is at least \$91 million, as evidenced by the NIH funding reports. This protein is only one of the many proteins which contain a metal ion cofactor. It is expected that a device which could solve the problems discussed here could likely provide interesting insights into other metalloproteins, such as FeMoco [4, 5]. The smallest problem of practical interest, that of the His6 binding site interacting with a copper ion, would require 7 million physical qubits with a run time of a little over 28 years. This points to the need to reduce overheads across the board, from a more compact chemical description, to better quantum algorithms, better error correction schemes, and faster physical operations. For the AB16 chemical description, active spaces may be an area to potentially create a more compact chemical description, though active space selection has to be carefully considered to maintain accuracy.

## ACKNOWLEDGEMENTS

This material is based upon work supported by the Defense Advanced Research Projects Agency under Contract No. HR001122C0074. Any opinions, findings and conclusions or recommendations expressed in this material are those of the authors and do not necessarily reflect the views of the Defense Advanced Research Projects Agency. This work is supported by Wellcome Leap as part of the Quantum for Bio Program. ZW acknowledges support from DARPA under IAA 8839, Annex 130 through NASA Academic Mission Services (contract NNA16BD14C).

The authors thank John Carpenter for his support in creating high-resolution figures for this paper.

- 
- [1] Y. Lu, N. Yeung, N. Sieracki, and N. M. Marshall, Design of functional metalloproteins, *Nature* **460**, 855 (2009).
  - [2] S. Lloyd, Universal quantum simulators, *Science* **273**, 1073 (1996).
  - [3] Y. Cao, J. Romero, J. P. Olson, M. Degroote, P. D. Johnson, M. Kieferová, I. D. Kivlichan, T. Menke, B. Peropadre, N. P. Sawaya, *et al.*, Quantum chemistry in the age of quantum computing, *Chemical reviews* **119**, 10856 (2019).
  - [4] M. Reiher, N. Wiebe, K. M. Svore, D. Wecker, and M. Troyer, Elucidating reaction mechanisms on quantum computers, *Proceedings of the National Academy of Sciences* **114**, 7555 (2017).
  - [5] Z. Li, J. Li, N. S. Dattani, C. Umrigar, and G. K.-L. Chan, The electronic complexity of the ground-state of the fmo cofactor of nitrogenase as relevant to quantum simulations, *The Journal of Chemical Physics* **150**, 024302 (2019).
  - [6] M. Otten, B. Kang, D. Fedorov, J.-H. Lee, A. Be-

- nali, S. Habib, S. K. Gray, and Y. Alexeev, Qrechem: quantum resource estimation software for chemistry applications, *Frontiers in Quantum Science and Technology* **2**, 1232624 (2023).
- [7] S. K. T. S. Wärmländer, N. Österlund, C. Wallin, J. Wu, J. Luo, A. Tiiman, J. Jarvet, and A. Gräslund, Metal binding to the amyloid- $\beta$  peptides in the presence of biomembranes: potential mechanisms of cell toxicity, *JBIC Journal of Biological Inorganic Chemistry* **24**, 1189 (2019).
- [8] B. Strodel and O. Coskuner-Weber, Transition metal ion interactions with disordered amyloid- $\beta$  peptides in the pathogenesis of alzheimer's disease: Insights from computational chemistry studies, *Journal of Chemical Information and Modeling* **59**, 1782 (2019), pMID: 30933519, <https://doi.org/10.1021/acs.jcim.8b00983>.
- [9] D. Shea and V. Daggett, Amyloid- $\beta$  oligomers: Multiple moving targets, *Biophysica* **2**, 91 (2022).
- [10] L. M. Miller, Q. Wang, T. P. Telivala, R. J. Smith, A. Lanzirrotti, and J. Miklossy, Synchrotron-based infrared and x-ray imaging shows focalized accumulation of cu and zn colocalized with  $\beta$ -amyloid deposits in alzheimer's disease, *Journal of Structural Biology* **155**, 30 (2006).
- [11] H. Kozłowski, M. Luczkowski, M. Remelli, and D. Valensin, Copper, zinc and iron in neurodegenerative diseases (alzheimer's, parkinson's and prion diseases), *Coordination Chemistry Reviews* **256**, 2129 (2012), metal Ions in Neurodegenerative Diseases.
- [12] S. Zirah, S. A. Kozin, A. K. Mazur, A. Blond, M. Cheminant, I. Ségalas-Milazzo, P. Debey, and S. Rebuffat, Structural changes of region 1-16 of the alzheimer disease amyloid  $\beta$ -peptide upon zinc binding and in vitro aging, *The Journal of Biological Chemistry* **281**, 2151 (2006).
- [13] 2024 alzheimer's disease facts and figures, *Alzheimer's & Dementia* **n/a**, <https://alz-journals.onlinelibrary.wiley.com/doi/pdf/10.1002/alz.13809>.
- [14] N/A, *Nih reporter* (2023).
- [15] S. Azimi and A. Rauk, The binding of fe (ii)-heme to the amyloid beta peptide of alzheimer's disease: Qm/mm investigations, *Journal of Chemical Theory and Computation* **8**, 5150 (2012).
- [16] K. Kitaura, E. Ikeo, T. Asada, T. Nakano, and M. Uebayasi, Fragment molecular orbital method: an approximate computational method for large molecules, *Chemical Physics Letters* **313**, 701 (1999).
- [17] T. H. Dunning Jr, Gaussian basis sets for use in correlated molecular calculations. i. the atoms boron through neon and hydrogen, *The Journal of chemical physics* **90**, 1007 (1989).
- [18] T. Nakano, T. Kaminuma, T. Sato, Y. Akiyama, M. Uebayasi, and K. Kitaura, Fragment molecular orbital method: application to polypeptides, *Chemical Physics Letters* **318**, 614 (2000).
- [19] T. Nagata, D. G. Fedorov, and K. Kitaura, Importance of the hybrid orbital operator derivative term for the energy gradient in the fragment molecular orbital method, *Chemical Physics Letters* **492**, 302 (2010).
- [20] A. Y. Kitaev, Quantum measurements and the abelian stabilizer problem, arXiv preprint [quant-ph/9511026](https://arxiv.org/abs/quant-ph/9511026) (1995).
- [21] G. Ortiz, J. E. Gubernatis, E. Knill, and R. Laflamme, Quantum algorithms for fermionic simulations, *Phys. Rev. A* **64**, 022319 (2001).
- [22] R. Babbush, J. McClean, D. Wecker, A. Aspuru-Guzik, and N. Wiebe, Chemical basis of Trotter-Suzuki errors in quantum chemistry simulation, *Phys. Rev. A* **91**, 022311 (2015).
- [23] G. H. Low and I. L. Chuang, Hamiltonian simulation by qubitization, *Quantum* **3**, 163 (2019).
- [24] V. von Burg, G. H. Low, T. Häner, D. S. Steiger, M. Reiher, M. Roetteler, and M. Troyer, Quantum computing enhanced computational catalysis, *Physical Review Research* **3**, 033055 (2021).
- [25] R. Babbush, C. Gidney, D. W. Berry, N. Wiebe, J. McClean, A. Paler, A. Fowler, and H. Neven, Encoding electronic spectra in quantum circuits with linear t complexity, *Phys. Rev. X* **8**, 041015 (2018).
- [26] D. W. Berry, C. Gidney, M. Motta, J. R. McClean, and R. Babbush, Qubitization of Arbitrary Basis Quantum Chemistry Leveraging Sparsity and Low Rank Factorization, *Quantum* **3**, 208 (2019).
- [27] Q. Sun, T. C. Berkelbach, N. S. Blunt, G. H. Booth, S. Guo, Z. Li, J. Liu, J. D. McClain, E. R. Sayfutyarova, S. Sharma, *et al.*, Pyscf: the python-based simulations of chemistry framework, *Wiley Interdisciplinary Reviews: Computational Molecular Science* **8**, e1340 (2018).
- [28] M. E. Beverland, P. Murali, M. Troyer, K. M. Svore, T. Hoefler, V. Kliuchnikov, G. H. Low, M. Soeken, A. Sundaram, and A. Vasshillo, Assessing requirements to scale to practical quantum advantage, arXiv preprint [arXiv:2211.07629](https://arxiv.org/abs/2211.07629) (2022).
- [29] W. van Dam, M. Mykhailova, and M. Soeken, Using Azure Quantum Resource Estimator for Assessing Performance of Fault Tolerant Quantum Computation, in *Proceedings of the SC '23 Workshops of The International Conference on High Performance Computing, Network, Storage, and Analysis*, SC-W '23 (Association for Computing Machinery, New York, NY, USA, 2023) p. 1414–1419.
- [30] Microsoft, *Azure Quantum Development Kit*.
- [31] A. G. Fowler, M. Mariantoni, J. M. Martinis, and A. N. Cleland, Surface codes: Towards practical large-scale quantum computation, *Physical Review A* **86**, 032324 (2012).
- [32] S. Bravyi and A. Kitaev, Universal quantum computation with ideal clifford gates and noisy ancillas, *Physical Review A* **71**, 022316 (2005).

Fragment	Basis	$N_{\text{orb}}$	$N_{\text{Q,logical}}$	$T_{\text{count}}$	Distance	$N_{\text{Q,physical}}$	$N_{\text{Tfactories}}$	$N_{\text{Q,factory}}$	Runtime (s)
8	sto-3g	23	661	4.00e10	15	8.68e5	15	2.40e5	2.31e5
1	sto-3g	30	820	9.29e10	15	1.01e6	15	2.40e5	5.38e5
7	sto-3g	35	923	1.72e11	15	1.11e6	15	2.40e5	9.97e5
0	sto-3g	36	942	1.87e11	15	1.13e6	15	2.40e5	1.09e6
6	sto-3g	44	1099	3.90e11	15	1.27e6	15	2.40e5	2.28e6
11	sto-3g	44	1099	3.28e11	15	1.27e6	15	2.40e5	1.92e6
2	sto-3g	51	1290	6.20e11	17	1.76e6	13	2.08e5	4.11e6
10	sto-3g	51	1290	6.51e11	17	1.76e6	13	2.08e5	4.31e6
14	sto-3g	53	1330	6.87e11	17	1.81e6	13	2.08e5	4.56e6
5	sto-3g	57	1413	9.37e11	17	1.90e6	13	2.08e5	6.23e6
12	sto-3g	57	1413	9.01e11	17	1.90e6	13	2.08e5	5.99e6
13	sto-3g	57	1413	9.06e11	17	1.90e6	13	2.08e5	6.02e6
8	6-31g*	62	1513	1.46e12	17	2.02e6	13	2.08e5	9.74e6
3	sto-3g	64	1553	1.32e12	17	2.07e6	13	2.08e5	8.76e6
4	sto-3g	68	1634	1.68e12	17	2.18e6	14	2.24e5	1.12e7
9	sto-3g	69	1654	1.74e12	17	2.20e6	14	2.24e5	1.16e7
8	cc-pvdz	71	1699	2.56e12	17	2.26e6	14	2.24e5	1.71e7
15	sto-3g	73	1736	2.18e12	17	2.30e6	14	2.24e5	1.45e7
5+Cu	sto-3g	77	1903	3.75e12	17	2.50e6	14	2.24e5	2.50e7
1	6-31g*	80	1966	3.92e12	17	2.57e6	14	2.24e5	2.62e7
7	6-31g*	94	2260	7.24e12	17	2.92e6	14	2.24e5	4.86e7
1	cc-pvdz	95	2281	7.95e12	17	2.94e6	14	2.24e5	5.33e7
0	6-31g*	96	2302	7.82e12	17	2.96e6	14	2.24e5	5.25e7
7	cc-pvdz	109	2585	1.37e13	17	3.30e6	14	2.24e5	9.19e7
0	cc-pvdz	114	2690	1.65e13	17	3.42e6	14	2.24e5	1.11e8
11	6-31g*	116	2734	1.62e13	17	3.47e6	14	2.24e5	1.09e8
6	6-31g*	120	2938	1.87e13	19	4.56e6	13	2.08e5	1.41e8
6	cc-pvdz	132	3203	2.78e13	19	4.95e6	13	2.08e5	2.09e8
10	6-31g*	138	3338	3.28e13	19	5.15e6	13	2.08e5	2.47e8
2	6-31g*	138	3338	3.18e13	19	5.15e6	13	2.08e5	2.39e8
14	6-31g*	142	3426	3.55e13	19	5.28e6	13	2.08e5	2.67e8
11	cc-pvdz	143	3448	3.98e13	19	5.31e6	13	2.08e5	3.00e8
13	6-31g*	154	3697	5.06e13	19	5.67e6	13	2.08e5	3.81e8
5	6-31g*	154	3697	5.12e13	19	5.67e6	13	2.08e5	3.86e8
12	6-31g*	154	3697	5.01e13	19	5.67e6	13	2.08e5	3.77e8
10	cc-pvdz	156	3741	5.46e13	19	5.74e6	13	2.08e5	4.12e8
2	cc-pvdz	156	3741	5.34e13	19	5.74e6	13	2.08e5	4.02e8
14	cc-pvdz	166	3961	6.84e13	19	6.06e6	13	2.08e5	5.16e8
3	6-31g*	172	4093	7.78e13	19	6.25e6	13	2.08e5	5.87e8
13	cc-pvdz	175	4159	8.44e13	19	6.35e6	13	2.08e5	6.36e8
5	cc-pvdz	175	4159	8.56e13	19	6.35e6	13	2.08e5	6.46e8
12	cc-pvdz	175	4159	8.40e13	19	6.35e6	13	2.08e5	6.34e8
4	6-31g*	180	4269	9.17e13	19	6.51e6	13	2.08e5	6.91e8
9	6-31g*	186	4404	1.05e14	19	6.70e6	13	2.08e5	7.90e8
5+Cu	6-31g*	192	4728	1.17e14	19	7.18e6	13	2.08e5	8.83e8
3	cc-pvdz	199	4889	1.42e14	19	7.41e6	13	2.08e5	1.07e9
9	cc-pvdz	213	5211	1.81e14	19	7.92e6	14	2.51e5	1.37e9

TABLE I. Resource estimates for all fragments.



Fragment	Basis	$N_{\text{orb}}$	$N_{\text{Q,logical}}$	$T_{\text{count}}$	Distance	$N_{\text{Q,physical}}$	$N_{\text{Tfactories}}$	$N_{\text{Q,factory}}$	Runtime (s)
8	sto-3g	23	661	4.00e10	15	8.68e5	15	2.40e5	2.31e5
5	sto-3g	57	1413	9.37e11	17	1.90e6	13	2.08e5	6.23e6
5+Cu	sto-3g	77	1903	3.75e12	17	2.50e6	14	2.24e5	2.50e7
1	6-31g*	80	1966	3.92e12	17	2.57e6	14	2.24e5	2.62e7
7	6-31g*	94	2260	7.24e12	17	2.92e6	14	2.24e5	4.86e7
1	cc-pvdz	95	2281	7.95e12	17	2.94e6	14	2.24e5	5.33e7
14	6-31g*	142	3426	3.55e13	19	5.28e6	13	2.08e5	2.67e8
11	cc-pvdz	143	3448	3.98e13	19	5.31e6	13	2.08e5	3.00e8
5	6-31g*	154	3697	5.12e13	19	5.67e6	13	2.08e5	3.86e8
5	cc-pvdz	175	4159	8.56e13	19	6.35e6	13	2.08e5	6.46e8
12	cc-pvdz	175	4159	8.40e13	19	6.35e6	13	2.08e5	6.34e8
9	6-31g*	186	4404	1.05e14	19	6.70e6	13	2.08e5	7.90e8
5+Cu	6-31g*	192	4728	1.17e14	19	7.18e6	13	2.08e5	8.83e8
3	cc-pvdz	199	4889	1.42e14	19	7.41e6	13	2.08e5	1.07e9
9	cc-pvdz	213	5211	1.81e14	19	7.92e6	14	2.51e5	1.37e9

TABLE II. Resource estimates for selected fragments.

Fragment 13		
C	-3.462	-4.282 1.523
O	-2.969	-4.629 0.451
N	-4.759	-4.103 1.729
H	-5.144	-3.768 2.588
C	-5.729	-4.392 0.687
H	-5.528	-5.408 0.346
C	-7.153	-4.362 1.247
H	-7.841	-4.835 0.513
H	-7.824	-4.836 0.531
N	-8.419	-2.681 2.673
H	-8.697	-3.335 3.378
C	-7.664	-2.973 1.551
C	-8.711	-1.389 2.656
H	-9.294	-0.854 3.406
N	-8.153	-0.846 1.536
C	-7.519	-1.801 0.868
H	-6.976	-1.672 -0.068

TABLE III. Geometry for fragment 13.

Fragment 4			
C	-8.802	4.408	-4.484
O	-8.920	3.816	-3.413
N	-7.956	5.403	-4.702
H	-7.906	5.928	-5.550
C	-7.006	5.815	-3.683
H	-6.821	4.951	-3.045
C	-5.752	6.305	-4.411
H	-6.053	6.812	-5.354
H	-6.054	6.856	-5.302
C	-4.793	5.186	-4.822
C	-4.072	4.527	-3.875
H	-4.177	4.797	-2.824
C	-3.182	3.488	-4.256
H	-2.604	2.960	-3.498
C	-3.051	3.152	-5.568
H	-2.368	2.354	-5.860
C	-4.663	4.849	-6.133
H	-5.241	5.377	-6.891
C	-3.773	3.811	-6.514
H	-3.668	3.541	-7.565

TABLE IV. Geometry for fragment 4.

Fragment 7			
C	-5.445	6.487	1.509
O	-4.556	5.789	1.995
N	-5.237	7.632	0.875
H	-5.940	8.227	0.494
C	-3.892	8.142	0.672
H	-3.339	7.319	0.220
C	-3.898	9.362	-0.251
H	-2.922	9.882	-0.175
H	-2.919	9.838	-0.206
C	-4.966	10.409	0.070
O	-5.599	10.266	1.139
O	-5.126	11.329	-0.761

TABLE V. Geometry for fragment 7.

Fragment 9			
C	-3.74	8.105	5.22
O	-3.733	8.271	6.439
N	-3.709	6.922	4.624
H	-3.712	6.807	3.631
C	-3.668	5.694	5.399
H	-4.566	5.655	6
H	-2.780	5.688	6.031

TABLE VI. Geometry for fragment 9.

Fragment 8			
C	-3.305	8.571	2.019
O	-2.087	8.614	2.184
N	-4.200	8.877	2.947
H	-5.191	8.841	2.819
C	-3.786	9.305	4.273
H	-2.790	9.728	4.141
C	-4.727	10.380	4.823
H	-5.710	9.902	5.037
H	-5.685	9.927	5.077
O	-4.934	11.436	3.889
H	-5.692	11.946	4.201

TABLE VII. Geometry for fragment 8.

Fragment 1			
N	-8.329	9.458	-6.956
H	-7.576	10.173	-6.893
H	-9.011	9.737	-7.690
H	-7.912	8.537	-7.202
C	-9.009	9.356	-5.676
H	-8.275	9.055	-4.929
C	-9.626	10.731	-5.416
H	-10.268	11.011	-6.275
H	-10.293	10.976	-6.243
C	-8.619	11.870	-5.247
O	-7.925	12.167	-6.243
O	-8.566	12.419	-4.125

TABLE VIII. Geometry for fragment 1.

Fragment 11			
C	-2.331	1.78	3.794
O	-1.704	1.695	4.849
N	-3.036	0.794	3.259
H	-3.519	0.843	2.389
C	-3.161	-0.488	3.933
H	-2.434	-0.461	4.744
C	-4.563	-0.662	4.522
H	-5.130	-1.364	3.868
H	-5.139	-1.348	3.901
C	-5.288	0.681	4.617
H	-5.969	0.672	5.487
H	-5.908	0.701	5.513
C	-6.160	0.922	3.383
O	-5.568	1.133	2.302
O	-7.399	0.891	3.548

TABLE IX. Geometry for fragment 11.

Fragment 5			
C	-7.57	6.959	-2.838
O	-7.103	8.093	-2.930
N	-8.566	6.621	-2.032
H	-8.980	5.714	-2.048
C	-9.109	7.569	-1.075
H	-8.814	8.548	-1.454
C	-10.634	7.466	-1.001
H	-10.924	6.606	-1.650
H	-10.974	6.623	-1.602
C	-11.295	8.753	-1.498
H	-11.073	8.869	-2.581
H	-11.033	8.921	-2.542
C	-10.858	9.954	-0.657
H	-11.741	10.601	-0.449
H	-11.717	10.589	-0.440
N	-9.827	10.731	-1.381
H	-10.066	11.107	-2.277
C	-8.593	10.961	-0.913
N	-8.250	10.537	0.311
H	-8.914	10.041	0.872
H	-7.332	10.715	0.664
N	-7.701	11.616	-1.669
H	-7.975	11.991	-2.554
H	-6.761	11.731	-1.347

TABLE X. Geometry for fragment 5.

Fragment 16			
C	-1.871	-2.898	-4.128
O	-2.849	-3.469	-4.607
N	-1.005	-2.177	-4.826
H	-0.209	-1.723	-4.429
C	-1.166	-1.997	-6.259
H	-1.546	-2.934	-6.666
C	-2.215	-0.920	-6.548
H	-3.079	-1.113	-5.870
H	-3.078	-1.064	-5.899
C	-2.657	-0.965	-8.012
H	-1.793	-0.696	-8.662
H	-1.816	-0.714	-8.658
C	-3.810	0.007	-8.267
H	-4.631	-0.225	-7.550
H	-4.632	-0.212	-7.585
C	-4.300	-0.089	-9.713
H	-3.499	0.228	-10.418
H	-3.499	0.199	-10.394
N	-5.476	0.785	-9.922
H	-5.210	1.739	-9.784
H	-5.819	0.666	-10.853
H	-6.193	0.541	-9.269
C	0.198	-1.711	-6.889
O	1.204	-1.674	-6.131
O	0.247	-1.527	-8.135

TABLE XI. Geometry for fragment 16.

Fragment 12			
C	-2.825	-1.629	2.97
O	-2.380	-1.389	1.849
N	-3.051	-2.845	3.444
H	-3.547	-3.042	4.286
C	-2.572	-4.023	2.740
H	-1.560	-3.811	2.396
C	-2.507	-5.214	3.698
H	-1.845	-4.947	4.521
C	-3.886	-5.522	4.284
H	-4.559	-5.837	3.486
H	-3.798	-6.319	5.022
H	-4.285	-4.627	4.763
C	-1.920	-6.445	3.003
H	-2.562	-6.732	2.170
H	-0.923	-6.210	2.630
H	-1.858	-7.268	3.714

TABLE XII. Geometry for fragment 12.

Fragment 15			
C	-3.372	-1.484	-2.018
O	-2.989	-0.596	-2.779
N	-2.765	-2.651	-1.862
H	-3.064	-3.364	-1.230
C	-1.577	-2.986	-2.629
H	-0.834	-2.238	-2.352
C	-1.055	-4.375	-2.253
H	-0.111	-4.530	-2.825
H	-0.124	-4.573	-2.783
C	-2.082	-5.457	-2.593
H	-3.066	-5.215	-2.137
H	-3.053	-5.184	-2.179
C	-1.650	-6.816	-2.039
O	-1.139	-7.669	-2.746
N	-1.883	-6.970	-0.739
H	-2.298	-6.226	-0.214
H	-1.642	-7.828	-0.286

TABLE XIII. Geometry for fragment 15.



Fragment 10			
C	-3.657	4.468	4.484
O	-4.668	3.780	4.350
N	-2.502	4.231	3.878
H	-1.686	4.799	3.976
C	-2.339	3.087	2.998
H	-3.179	3.075	2.303
C	-0.979	3.266	2.321
H	-0.863	4.328	2.011
H	-0.848	4.317	2.065
C	-0.798	2.422	1.057
C	-0.690	1.049	1.154
H	-0.734	0.566	2.130
C	-0.519	0.255	-0.035
H	-0.432	-0.829	0.027
C	-0.468	0.889	-1.237
O	-0.306	0.140	-2.360
H	-0.387	0.718	-3.172
C	-0.742	3.033	-0.179
H	-0.827	4.117	-0.255
C	-0.571	2.239	-1.368
H	-0.525	2.709	-2.350

TABLE XIV. Geometry for fragment 10.

Fragment 2			
C	-10.126	8.311	-5.73
O	-10.623	7.875	-4.693
N	-10.487	7.941	-6.950
H	-10.072	8.303	-7.784
C	-11.539	6.958	-7.152
H	-12.480	7.410	-6.839
C	-11.631	6.608	-8.639
H	-11.935	7.491	-9.202
H	-10.657	6.269	-8.993
H	-12.366	5.816	-8.781

TABLE XV. Geometry for fragment 2.

Fragment 14			
C	-5.531	-3.425	-0.481
O	-6.074	-3.636	-1.565
N	-4.752	-2.386	-0.222
H	-4.214	-2.290	0.614
C	-4.628	-1.289	-1.167
H	-5.505	-1.332	-1.813
C	-4.649	0.058	-0.442
H	-5.062	-0.087	0.580
H	-5.045	-0.088	0.563
N	-6.539	1.755	-0.538
H	-6.834	1.647	0.412
C	-5.468	1.119	-1.139
C	-7.046	2.625	-1.399
H	-7.899	3.281	-1.221
N	-6.314	2.556	-2.548
C	-5.360	1.647	-2.392
H	-4.615	1.370	-3.139

TABLE XVI. Geometry for fragment 14.

Fragment 6			
C	-8.52	7.317	0.314
O	-8.905	7.969	1.284
N	-7.595	6.370	0.367
H	-7.316	5.823	-0.421
C	-6.910	6.060	1.610
H	-7.398	6.646	2.390
C	-7.074	4.581	1.967
H	-6.506	3.967	1.235
H	-6.507	3.981	1.255
N	-8.857	2.775	1.828
H	-8.227	1.999	1.781
C	-8.507	4.106	1.975
C	-10.178	2.682	1.876
H	-10.758	1.763	1.791
N	-10.683	3.936	2.053
C	-9.675	4.798	2.113
H	-9.765	5.876	2.250

TABLE XVII. Geometry for fragment 6.

Fragment 3			
C	-11.26	5.732	-6.281
O	-12.119	5.306	-5.509
N	-10.057	5.199	-6.432
H	-9.351	5.548	-7.042
C	-9.663	4.016	-5.687
H	-10.595	3.566	-5.344
C	-8.928	3.020	-6.586
H	-8.894	2.038	-6.061
H	-8.883	2.047	-6.098
C	-7.511	3.507	-6.899
H	-7.557	4.521	-7.335
H	-7.548	4.534	-7.263
C	-6.843	2.612	-7.945
O	-7.085	1.388	-7.883
O	-6.105	3.174	-8.783

TABLE XVIII. Geometry for fragment 3.